William Ebmeyer and Pratik P. Dholabhai*

School of Physics and Astronomy Rochester Institute of Technology Rochester, NY 14623

* Email: pratik.dholabhai@rit.edu

Title: High-throughput prediction of oxygen vacancy defect migration near misfit dislocations in SrTiO₃/BaZrO₃ heterostructures

William Ebmeyer and Pratik P. Dholabhai *Materials Advances*, 2024, **5**, 315-328 https://doi.org/10.1039/D3MA00850A

In the published version of the paper, the **Acknowledgments** was incomplete as the National Science Foundation (NSF) CAREER Award grant number 2042311 was acknowledged, whereas the complete award number is DMR-2042311. The author apologizes for any inconvenience that it may have caused.

High-throughput prediction of oxygen vacancy defect migration near misfit dislocations in SrTiO₃/BaZrO₃ heterostructures

William Ebmeyer and Pratik P. Dholabhai*

School of Physics and Astronomy Rochester Institute of Technology Rochester, NY 14623

* Email: <u>pratik.dholabhai@rit.edu</u>

Abstract

Among their numerous technological applications, semi-coherent oxide heterostructures have emerged as promising candidates for applications in intermediate temperature solid oxide fuel cell electrolytes, wherein interfaces influence ionic transport. Since misfit dislocations impact ionic transport in these materials, oxygen vacancy formation and migration at misfit dislocations in oxide heterostructures is central to its performance as an ionic conductor. Herein, we report High-throughput atomistic simulations to predict thousands of activation energy barriers for oxygen vacancy migration at misfit dislocations in SrTiO₃/BaZrO₃ heterostructures. Dopants display a noticeable effect as higher activation energies are uncovered in their vicinity. Interface layer chemistry has a fundamental influence on the magnitude of activation energy barriers since they are dissimilar at misfit dislocations as compared to coherent terraces. Lower activation energies are uncovered when oxygen vacancies migrate toward misfit dislocations, but higher energies when they hop away, revealing that oxygen vacancies would get trapped at misfit dislocations and impact ionic transport. Results herein offer atomic scale insights into ionic transport at misfit dislocations and fundamental factors governing ionic conductivity of thin film oxide electrolytes.

1. Introduction

Complex oxide heterostructures, ^{1,2,3} an intriguing class of materials fabricated by marrying two dissimilar oxides exhibit superior and emergent properties ^{4,5,6} than their individual constituents. They have found promising applications in a wide range of technologies that include Solid Oxide Fuel Cells (SOFCs),^{7,8} radiation tolerant nuclear materials,⁹ information storage,¹⁰ batteries,¹¹ and catalysts.¹² SOFCs are electrochemical conversion device that produce electricity directly from oxidizing a fuel.^{13,14,15} They are highly efficient and have the potential to achieve our society's ambition of transitioning from fossil fuels to clean generation of electrical power. Due to the ever-growing miniaturization of advanced nanotechnologies such as SOFCs, the role of surfaces and interfaces has never been more critical.

In SOFCs, solid ceramic oxide electrolyte is one of the most important components since it facilitates the passage of oxide ions from the cathode to the anode. Since high ionic conductivity is imperative for the development of next-generation SOFCs, significant research efforts have been dedicated toward the discovery and design of electrolytes that allow faster ionic diffusion. Since high operating temperatures lead to issues with stability and durability, widespread deployment of SOFC technology necessitates lowering the operating temperatures to the intermediate-temperature (IT-SOFC) range of 773–973 K. 7,16 One promising option to lower the operating temperature is via implementation of thin film oxide electrolytes (oxide heterostructures), which exhibit superior performance at lower temperatures and are poised to take over as the next-generation IT-SOFC electrolytes. However, their widespread use requires the basic understanding of the role of interfaces in shaping enhanced performance. 15,16

Depending on the lattice mismatch, in semi-coherent oxide heterostructures, misfit dislocations originate at the heterointerface to mitigate the misfit strain between the two mismatched oxides. Since misfit dislocations are inevitable and responsible for controlling vital material properties, 8,18,19,20 several studies have focused on investigating their role in semi-coherent oxide heterostructures. Nonetheless, their impact on ionic transport is not well understood since studies focused on elucidating the atomic and electronic structure of misfit dislocations are limited due to challenges in studying and characterizing individual columns of atoms at the heterointerface. Owing to their fundamental character and influence on material properties, recent computational and experimental studies have focused on thorough investigation of the structure-property relationships at misfit dislocations in oxides.

Perovskite oxide heterostructures have gained popularity due to their versatility in diverse technologies, including SOFCs. Depending on the desired application, perovskites are often doped to enhance magnetic, ²¹ ionic, ²² electronic, ²³ optical, and catalytic ²⁴ properties. Among various perovskite oxides, SrTiO₃ (STO)²⁵ and BaZrO₃ (BZO) have been frequently studied, wherein doping is used to tune their functionality. For instance, perovskite oxide heterostructures have been studied as model systems for understanding ionic transport across oxide interfaces. Due to the compositional flexibility of perovskite lattice (*ABO*₃), dopants can replace either *A*-site, *B*-site, or *O*-site ions. Since our present work is mainly focused on fundamental aspects of oxygen vacancy migration in STO/BZO heterostructures, we will limit the discussion to acceptor doping (*p*-type). ²⁶ Acceptor doping, wherein the *B*-site cations, either Ti⁴⁺ in STO or Zr⁴⁺ in BZO, could be replaced with trivalent dopants has been extensively studied in STO²⁷ and BZO²⁸ since it leads to the formation of oxygen vacancies to maintain the defect equilibria.

Widespread use of acceptor doping strategy in perovskites is evident from the literature, wherein a multitude of aliovalent dopants have been added to improve the properties of STO^{29,30,31,32,33,34,35,36} and BZO.^{28,37,38} Unfortunately, the added impurities do not come without challenges since they induce physical and chemical changes in the materials by segregating at surfaces and interfaces. Segregation behavior depends on size mismatch and charge interactions,³⁹ formation of space-charge layers at interfaces,⁴⁰ and on growth conditions and post-deposition annealing procedures.⁴¹ Since segregated additives could lead to deleterious effects on material stability and performance, the role of dopants and associated vacancies in complex oxides have been studied extensively. In fast ion conductors, the influence of dopants is even more critical since they are primarily introduced to increase the oxygen vacancy concentration, but their presence on the cation sublattice alters the oxygen vacancy migration barriers on the anion sublattice. Oxygen vacancy formation ⁴² and migration ^{43,44,45,46,47,48,49} in various perovskite oxides have been reported, wherein density functional theory (DFT) calculations and simulations based on interatomic potentials have been the method of choice. These results demonstrate how dopants can influence oxygen vacancy migration in bulk perovskites.

From a fundamental perspective, acceptor doping has been extensively used to improve the properties of bulk STO and bulk BZO. Nonetheless, in perovskite heterostructures, especially near misfit dislocations, how dopants influence the migration pathways of these vacancies is not well understood since majority of reported work is focused on either bulk STO or bulk BZO. At

interfaces, it is imperative to understand the basic role of trivalent dopants and associated oxygen vacancies that are responsible for ionic conduction. To the best of our knowledge, there are no studies in the literature that report oxygen vacancy migration near misfit dislocations in STO/BZO heterostructures. Since STO⁵⁰ and BZO²⁸ have key technologically applications that include SOFC electrolytes, 8,51,52,53 oxide heterostructures synthesized using either of them have garnered significant research interest. 54,55,56 To understand the ionic transport mechanisms in a model oxide heterostructure used for SOFC electrolytes, basic knowledge of oxygen vacancy migration pathways in the vicinity of misfit dislocations is crucial. One of the main reasons for the lack of understanding of ionic transport mechanisms is due to the challenges in experimentally visualizing dopant atoms, characterizing oxygen vacancies, and resolving the structure and chemistry of misfit dislocations. The problem is further compounded as even from a theoretical perspective, calculations that utilize DFT are limited to coherent interfaces to keep the supercell size tractable.⁵⁷ As a result, DFT calculations are not optimal to study oxygen vacancy migration at misfit dislocations, which necessitate very large supercells. In this regard, atomistic simulations based on empirical interatomic potentials are valuable in offering atomic scale insights of dopants and defects at misfit dislocations in oxide heterostructures.²⁹

In perovskite oxides, defects could typically introduce ligand holes, which could further lead to altered magnetic properties as observed in STO.⁵⁸ In addition, oxygen vacancy formation and migration in perovskites could be influenced by change in oxidation states of added impurities having mixed valence, which could offer routes for tailoring mixed ionic electronic conductors in SOFCs.⁵⁹ However, we strictly focus on studying the role of defects (oxygen vacancies) that are formed to maintain the defect equilibria after incorporation of trivalent dopants that do not exhibit mixed valence. As current work is focused on studying the qualitative behavior of interface governed ionic transport, emphasis on fixed ionic charges of metals (dopant and host) and resulting oxygen vacancies is rational since oxygen vacancy diffusion mechanism is the primary mechanism for ionic conductivity in SOFC electrolytes.^{7,8}

In cases where perovskite oxide heterostructures are implemented as model systems for SOFC electrolytes, knowledge of oxygen vacancy migration pathways in influencing the ionic transport would be beneficial. To achieve this goal, we used atomistic simulations in conjunction with high-throughput computing to predict thousands of activation energy barriers for oxygen vacancy migration in the model system of STO/BZO heterostructure, ⁶⁰ with emphasis on misfit

dislocations and interface region. We studied oxygen vacancy migration pathways at SrO–ZrO₂, BaO–TiO₂, and ZrO₂–TiO₂ interfaces having dissimilar misfit dislocation structures.⁶⁰ The main goal of this work is to offer atomic scale insights pertaining to the migration behavior of oxygen vacancies near misfit dislocations and shed light on the potential influence of differing misfit dislocation structures on ionic conductivity.

2. Methodology

Atomistic simulations with 3D periodic boundary conditions (PBC) were conducted within the framework of Large-scale Atomic/Molecular Massively Parallel Simulator (LAMMPS).⁶¹ The simulations are based on energy minimization using a classical Born-like description of an ionic solid. Parameterized Buckingham⁶² pair potentials given by **Equation 1** were utilized to describe the two-body short-range interactions, whereas interactions due to the long-range Coulombic (electrostatic) forces were calculated by means of Ewald's method.⁶³

$$U(r) = Ae^{\left(-\frac{r}{\rho}\right)} - \frac{C}{r^6} + \frac{q_1 q_2}{4\pi\epsilon_0 r} \tag{1}$$

Here, A, ρ , and C are the potential parameters fitted to match the experimental data for a given pair of atoms. The first two terms model Pauli repulsion and van der Waals attraction, respectively, whereas the last term represents the Coulomb potential between ions. These pair potentials are not polarizable, so charge fluctuations are not allowed within this formalism.

Parameters for the Buckingham pair potential as derived by Busker *et al.*⁶⁴ and Zacate *et al.*⁶⁵ were used for Sr^{2+} , Ti^{4+} , Ba^{2+} , Zr^{4+} , O^{2-} , and Gd^{3+} . These interatomic potential parameters were chosen since all the divalent, trivalent, and tetravalent cation interactions were fitted against the same O^{2-} potential. Though the potential parameters used in this work were derived for bulk perovskites, they are expected to qualitatively capture the interface effects. The methodology used in this work has been successfully used to study a wide variety of oxide heterostructures. 29,54,55,56,57,60

Atomic models of STO/BZO heterostructure were constructed for the experimentally observed cube-on-cube orientation relationship, wherein $(001)_{STO}||(001)_{BZO}||$ interface and $[010]_{STO}||[010]_{BZO}$. Since lattice parameters are $a_{STO} = 3.905$ Å and $a_{BZO} = 4.197$ Å, the lattice

mismatch (~7.0%, computed with respect to a BZO substrate) resulting from this orientation relationship is accommodated via the formation of misfit dislocations at the heterointerface. In these atomic models, 14 unit cells of STO were matched with 13 unit cells of BZO to ensure a heterostructure with negligible amount of extrinsic strain. The supercell model for heterostructures comprise of 21,900 atoms. Via cleaving STO at either the neutral SrO or TiO₂ layer and BZO at either the neutral BaO or ZrO₂ layer, there are four combinations of heterointerfaces possible, namely SrO–BaO, SrO–ZrO₂, TiO₂–BaO, and TiO₂–ZrO₂. For these four fully stoichiometric heterostructures, constant temperature and pressure (NPT) simulations were performed using the conjugate gradient method for internal coordinate and stress minimization using the Nosé-Hoover thermostat at 0 K and zero pressure to obtain a relaxed structure free from internal stresses. The 0 K relaxed structures were further annealed at 1000 K.

A wide variety of trivalent dopants can be added to improve the properties of perovskites, as they have a net effective charge that affects the electroneutrality condition, and thereby the defect equilibria. 29,30,31,37 In perovskites, trivalent dopants can replace either of the cations on the A and B sublattices. For instance, in STO and BZO, donor doping (n-type) can be carried out by replacing Sr^{2+} or Ba^{2+} with trivalent dopants, whereas replacing Ti^{4+} or Zr^{4+} with trivalent dopants leads to acceptor doping (p-type). Since the current work is focused on ionic transport in perovskite heterostructures, we have exclusively studied acceptor doping. The defect reaction governing the addition of trivalent dopants to TiO_2 (STO) or ZrO_2 layer (BZO) can be expressed in Kröger–Vink notation as:

$$M_2 O_3 \xrightarrow{BO_2} 2M_B' + V_0'' + 3O_0^{\times}$$
 (2)

where $V_0^{"}$, B, and M correspond to the oxygen vacancy, B-site cations (either Ti^{4+} or Zr^{4+}) and trivalent dopants (Gd^{3+}), respectively. Owing to ionic compensation, this reaction indicates that the substitution of two B-site cations with trivalent dopants will result in the formation of one oxygen vacancy. The formation and migration of oxygen vacancy is at the heart of our work, so we will strictly focus on its migration in the vicinity of Gd^{3+} dopants at various interfaces for diverse nearest neighbor scenarios. In p-type oxides used for catalysis, surface oxygen vacancies become doubly positively charged, which lowers their formation energy and results in a higher defect concentration.⁶⁷ In addition, this study reports that space-charge regions impact the

concentration of oxygen vacancies at oxide surfaces. The type of vacancy in this study⁶⁷ is consistent with the current work. However, studying the fundamental impact of space-charge regions at such complex interfaces is beyond the scope of this work since we study doping scenarios that result in dilute oxygen vacancy concentration. Furthermore, we explicitly study the role of oxygen vacancies in the neighborhood of trivalent dopants, which is not the case in the study by Richter *et al.*,⁶⁷ since it neglects the role of dopant-defect clusters.

It is anticipated that DFT calculations would offer better description of migration pathways by including electronic effects in perovskites. However, these calculations are beyond the scope of this work primarily due to computational time and system size, both of which enter the realm of the impossible when it comes to employing DFT since the supercell size in this work is \sim 9.88 \times 5.47 \times 5.47 nm³ (21,900 atoms). Furthermore, we recently computed the electronic structure and predicted the atomic scale structure of misfit dislocations at CeO₂/MgO heterostructures using DFT⁶⁸ and compared it with atomistic simulations.⁶⁹ We found that the atomic structure and qualitative trends for dopant-defect cluster stability predicted using DFT and atomistic simulations agree very well. This agreement not only validates the current approach, but also reveals that the underlying assumptions of the method remain truthful.

A usual critique of the methodology based on interatomic potentials used in this work is that they are unsuitable for chemical environments for which they are not fitted against, such as interfaces and transition states for migration barrier calculations. However, it is important to note that we have rigorously tested the methodology implemented in this work and successfully utilized it to understand the thermodynamics and kinetics of defects at interfaces, ^{29,54,55,60,69,70} surfaces, ^{71,72} steps, ^{56,73} and grain boundaries ^{74,75,76} in complex oxides. In addition, we have effectively used this methodology to study structure-property relationships at misfit dislocations, as well as compute migration barriers in intricate chemical environment. ⁵⁵ Crucially, we have used classical forcefields to interpret the experimental observations by predicting qualitative structure-property trends and basic mechanisms at oxide interfaces, which includes perovskites.

To tackle the computation of vast amount of activation energy barriers at asymmetric interfaces, hundreds for a single interface, and hundreds of thousands for an entire structure, we developed a high-throughput framework using both custom software tools and LAMMPS. High-throughput nudged elastic band (NEB) simulations were performed to map out energy barriers for oxygen vacancy jumps in many possible scenarios. Initial effort was focused on mapping out all

nearest-neighbor jumps within one doped interface layer at a time. However, later scenarios eventually moved to mapping such barriers across the entire structure. This framework enabled rapid preparation and mapping of entire scenarios with varying interface chemistry and placement of dopants and vacancies. The approach starts by assigning ten dopants and five resulting vacancies. Later, energy minimization was performed before passing the result onto high-throughput NEB simulations, wherein one moving and four static oxygen vacancies were assigned to the structure, and the NEB simulation was allowed to run its course. Each NEB trajectory consisted of seven replicas with energy and force tolerances of 10^{-6} eV and 10^{-6} eV/Å, respectively.

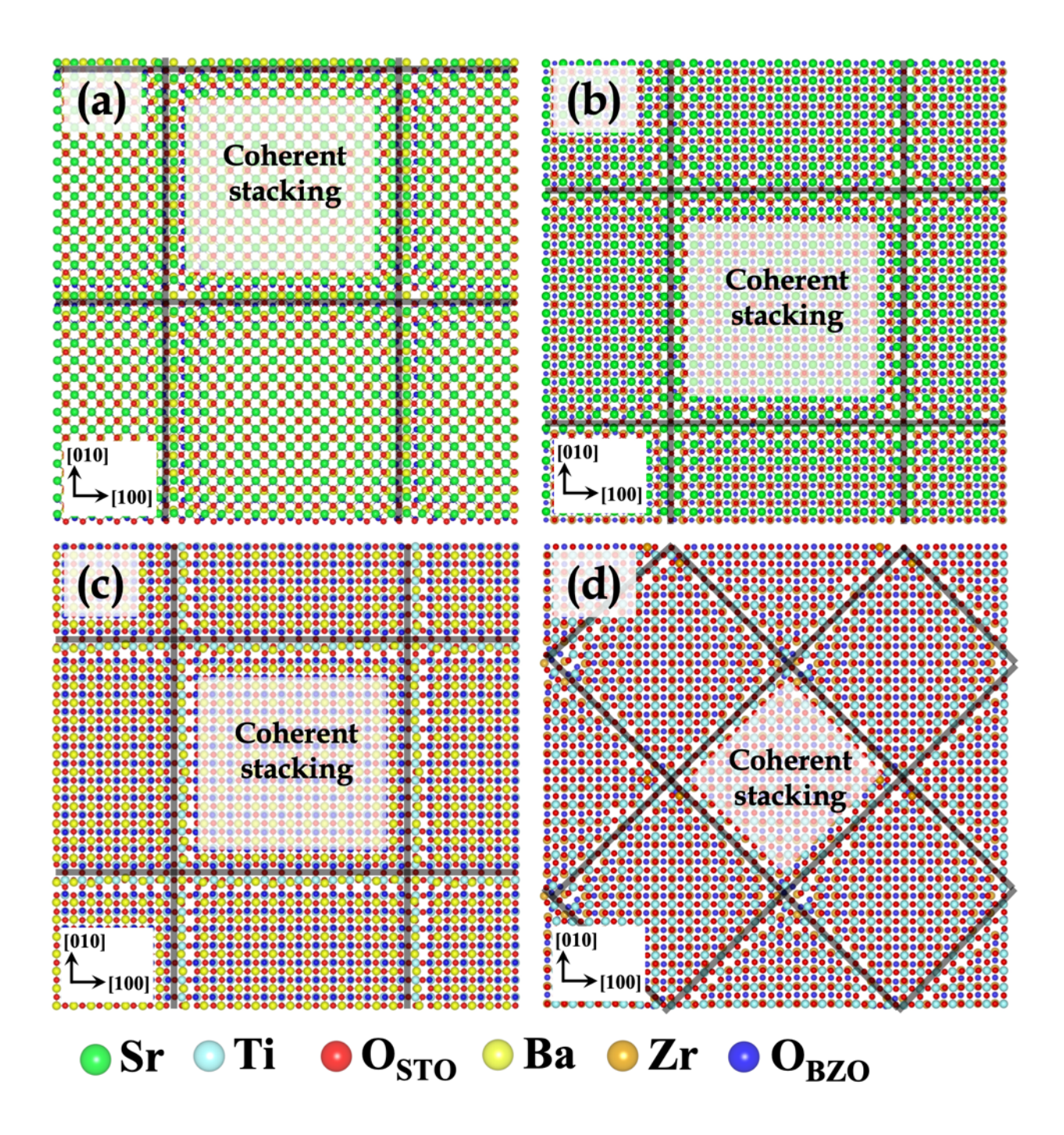
3. Results & Discussion

3.1 Atomic scale structure of the interface

In STO/BZO heterostructures having experimentally observed cube-on-cube orientation relationship, four different types of interfaces are possible depending on the interface layer chemistries involved in the formation of the interface. **Figure 1** depicts the minimized and subsequently annealed structures of four possible STO/BZO interfaces, which are SrO-BaO, SrO-ZrO₂, BaO-TiO₂, and ZrO₂-TiO₂ interfaces. In **Figure 1**, the heterostructures are shown along the interface normal direction with the relaxed supercells extended in the *x* and *y* direction (2 × 2 × 1) to clearly illustrate the misfit dislocation network indicated via black lines. We predict that SrO-BaO, SrO-ZrO₂, and TiO₂-BaO interfaces have a dislocation structure with Burgers vector of $\vec{b} = \langle 100 \rangle$, whereas TiO₂-ZrO₂ interface exhibits a misfit dislocation structure with Burgers vector of $\vec{b} = \langle 110 \rangle$, which is in agreement with the qualitative prediction reported using a heuristic approach.⁶⁰ While experiments have reported perovskite heterostructures with cube-on-cube epitaxy, ^{18,66,77} dependence of misfit dislocation structure on interface layer chemistry is not well understood. Since these differing misfit dislocation structures as a function of interface chemistry are expected to influence interface-governed properties, ^{29,54} these results reveal the importance of understanding such fundamental aspects of interface formation.

Figure 1. Minimized and subsequently annealed STO/BZO interfaces. (a) SrO-BaO interface (b) $SrO-ZrO_2$ interface (c) $BaO-TiO_2$ interface and (d) TiO_2-ZrO_2 interface. The view is normal to the interface plane. In (a), (b), and (d), STO layer is shown on top, whereas in (c), BZO layer is show on top for better contrast. Coherent stackings are shown for clarity. Black lines indicate the

misfit dislocation network. Atomic colors are given below the figure panel. Oxygen ions in STO and BZO are colored differently for clarity.



A closer inspection of the minimized interface atomic arrangement reveals that there are commonalities as well as dissimilarities between the four interfaces. The four STO/BZO heterostructures (**Figure 1**) constitute different types of bonding and atomic stacking at the

interface. The coherent stackings were distinguished from the misfit dislocations based on disregistry of atoms in a single layer across the interface. In all the cases, coherent stackings were identified roughly within 1-2 lattice constants of the visibly dislocated area. From here on, we will refer to O_{STO} (red) and O_{BZO} (blue) as oxygen atoms in STO and BZO layers, respectively. To describe the various stackings, atomic pairs across the interface will be denoted by $\{\ /\ \}$ notation. That is, $\{Sr/O_{BZO}\}$ indicates that Sr atom from STO is coordinated (paired) with oxygen atom in BZO. Notation [] will indicate that the particular atomic species does not have any coordinating atom (nearest neighbor bonding species) across the interface.

For the four interfaces (**Figure 1**), the coherent terrace comprises of the following nearest neighbor environments: (i) SrO–BaO interface: {Sr/O_{BZO}} and {O_{STO}/Ba} (ii) SrO–ZrO₂ interface: {Sr/[]}, {O_{STO}/Zr}, and {[]/O_{BZO}} (iii) TiO₂–BaO interface: {Ti/O_{BZO}}, {O_{STO}/[]}, and {[]/Ba} (iv) TiO₂–ZrO₂ interface: {Ti/O_{BZO}}, {O_{STO}/Zr}, {[]/O_{BZO}}, and {O_{STO}/[]}. Evidently, the coherent terraces constitute favorable electrostatic interactions at the four interfaces. The intermediate regions separating the coherent terraces consist of the misfit dislocations lines and intersections. In contrast to the coherent terraces, they exhibit favorable (anion–cation) as well as unfavorable (cation–cation and anion–anion) electrostatic interactions. Repulsive interactions lead to chemical frustration at the interface, which are often conducive to defect formation. S4,56 Such intricate interface chemical bonding due to the existence of misfit dislocations is observed in other semi-coherent oxide interfaces but has not received much attention in semi-coherent perovskite-perovskite interfaces. 60

3.2 Defect migration at interfaces

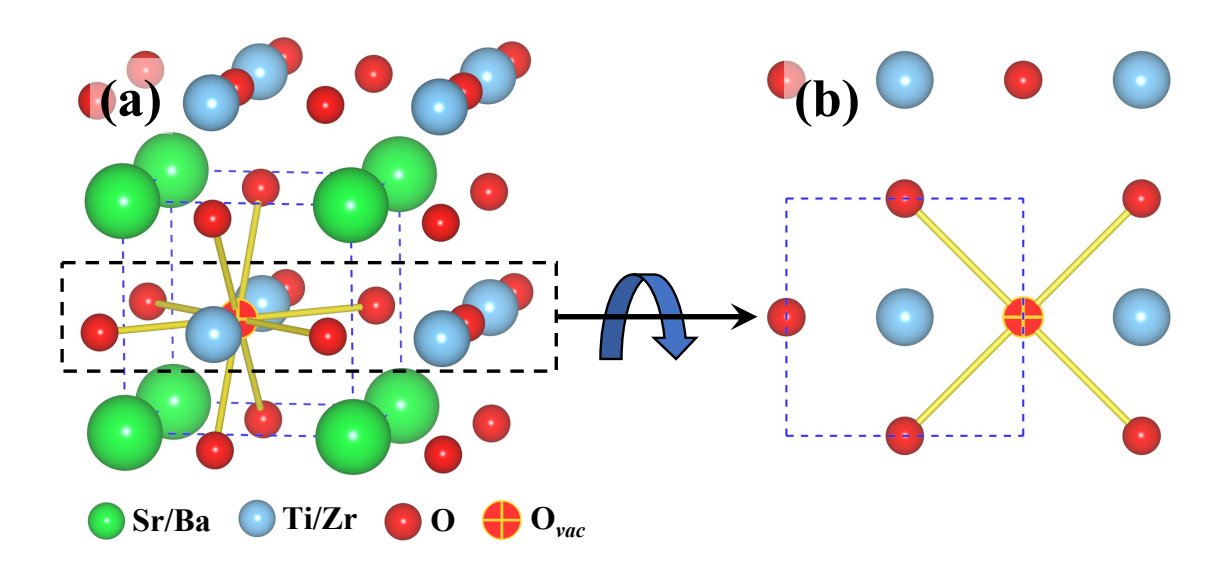
Oxygen vacancy formation and migration in SOFC electrolytes is fundamental to its performance as an ionic conductor. We have used STO/BZO as a model system to study oxygen vacancy migration at interfaces and elucidate the influence of misfit dislocations on ionic transport in thin film oxide electrolytes. To investigate the fundamental factors influencing the ionic conductivity at interfaces, we have developed a high-throughput strategy to compute thousands of nearest neighbor activation energies for oxygen vacancy migration in the vicinity of Gd³⁺ dopants at STO/BZO interfaces. The computation of the rate of these events will facilitate the future development of a kinetic lattice Monte Carlo (KLMC) model⁷⁸ for vacancy diffusion at oxide heterointerfaces, which will further allow for determination of oxygen ion conductivity. Although the migration energy barriers are calculated at 0 K, temperature effects will be included in the

KLMC simulations to understand the trends in ionic conductivity as a function of temperature. We have used a similar strategy to study and design bulk electrolyte materials as well as compare with experimental observations.^{78,79}

As mentioned earlier, we strictly focus on doping the TiO₂ or ZrO₂ layer for ionic conductivity applications. Moreover, since we are primarily interested in the interplay between dopants and oxygen vacancies precisely at the interface layer, SrO-BaO interface has not been considered for studying oxygen vacancy migration. For SrO-ZrO₂, TiO₂-BaO, and TiO₂-ZrO₂ (both sides) interfaces, we studied 4 different configurations for placing 10 dopants and resulting 5 vacancies. Among these configurations, 3 were chosen with dopants placed as nearest neighbors, whereas in the fourth configuration, dopants were isolated. In a large heterostructure supercell with thousands of cations and anions, (21,900 atoms in the current system) 10 dopants indicate a rather dilute doping limit. Since we have deliberately placed all the dopants at the interface layer, the dopant fraction of the interface layer is bit higher ranging from 1.7 - 1.9%, which is nevertheless in the dilute limit, but reasonable for comparison with realistic scenarios. Nonetheless, the low dopant and vacancy fraction studied in this work can assist in unravelling the atomic scale mechanisms for vacancy migration at interfaces. Via high-throughput simulations, for each of these interface configurations, ~1000-1400 nearest neighbor barriers were computed for single side of the interface. In two different cases, the full structure was studied, which accounted for ~100000 nearest neighbor barriers. In total, ~250,000 activation energy barriers were computed to obtain a comprehensive understanding of oxygen vacancy migration.

Given in **Figure 2a** are 8 possible nearest neighbor jump directions for the oxygen vacancy starting from BO_2 (B = Ti, Zr) layer. In **Figure 2b**, normal view of the BO_2 layer is offered, which depicts the 4 nearest neighbor pathways for in-layer migration of an oxygen vacancy. Since the focus is on understanding BO_2 layer migration pathways specifically at the interface, data showing activation energy barriers for oxygen vacancy migration will be shown for the network consisting of the 4 pathways given in **Figure 2b**. It is important to note that though activation energy barriers were computed for vacancy migration throughout the supercell, we limit the discussion to interface layer. This strategy ensures that we capture the effect of misfit dislocations and their interplay with dopants and oxygen vacancies.

Figure 2. (a) Possible 8 nearest neighbor jump directions for an oxygen vacancy in either TiO_2 (STO) layer or ZrO_2 (BZO) layer are shown. (b) Normal view for the TiO_2 or ZrO_2 layer depicting the 4 nearest neighbor in-layer jump directions. These 4 directions will be used in following figures to show the magnitude of activation energy barriers on each side of the heterointerface. Atomic color scheme is given below the figure.

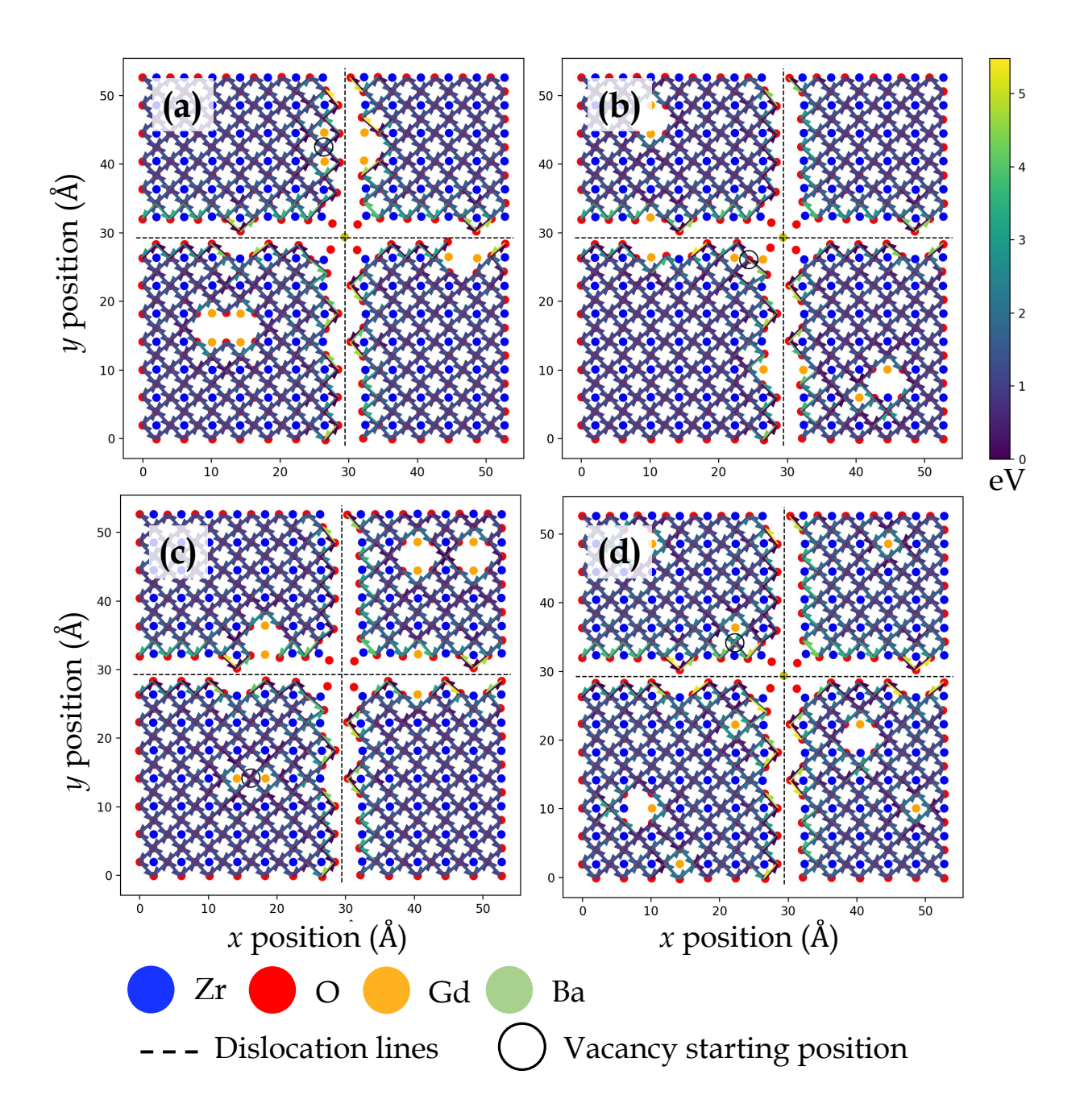


Figures 3, 4, 5, and 6 display the activation energies for nearest neighbor oxygen vacancy migration jumps in the vicinity of different dopant distributions at ZrO₂ side of SrO–ZrO₂, TiO₂ side of TiO₂–BaO, TiO₂ side of TiO₂–ZrO₂, and ZrO₂ side of TiO₂–ZrO₂ interfaces, respectively. Migration barriers connecting longer jumps (longer than the next nearest neighbor vacancy hops) across the misfit dislocations were not computed, which is evident in all figures. In these figures, for respective configurations given in a, b, and c, the gadolinium dopants are placed in nearest neighbor pairs, whereas in d, they are isolated. The primary reason to place dopants in pairs at nearest neighbors to the oxygen vacancy is that this configuration was found to be most favorable energetically at misfit dislocations in STO/BZO heterostructures.⁷⁰ Activation energies for oxygen vacancy migration are depicted via arrows pointing in a particular jump direction and their colors indicate the absolute magnitude given in the respective energy scale. The activation energies reported in this work are bit higher in magnitude, especially near misfit dislocations. However, interfaces are likely to induce such high barriers since high activation energy barriers from DFT have also been recently reported for perovskite surfaces.⁴⁸ Furthermore, activation energies for

oxygen vacancy migration in bulk STO and bulk BZO were found to be 1.20 eV and 1.0 eV, respectively. The computed value for STO is in reasonable agreement with reported DFT,⁸⁰ atomistic simulations,⁸¹ and experimental values,⁸² which offers confidence in the current method. In addition, it has been shown that the methodology used in this work is effective in predicting transport mechanisms in perovskites.⁸³ Vitally, the main aim of this work is to offer physically meaningful qualitative trends to describe the behavior of oxygen vacancies at misfit dislocations, which necessitate large supercells that are not feasible in DFT calculations.⁵⁷ In this section, we will strictly focus on qualitative trends and discuss their implications.

TiO₂–BaO and SrO–ZrO₂ interfaces have comparable chemical environments due to AO– BO_2 interface chemistry. At the ZrO₂ side of SrO–ZrO₂ interface (**Figure 3**), throughout the coherent (**Figure 1b**) terrace (stacking), activation energies are comparable in magnitude. Analogously, at the TiO₂ side of TiO₂–BaO interface (**Figure 4**), activation energies are more or less similar in magnitude throughout the coherent terrace (**Figure 1c**). This can be understood in terms of similar nearest neighbor environment in coherent terraces in SrO–ZrO₂ and TiO₂–BaO interfaces. For respective coherent regions in SrO–ZrO₂ and TiO₂–BaO interfaces, O_{BZO} and O_{STO} do not have a nearest neighbor cation or anion across the interface, which results in similar barrier heights when oxygen vacancies hop around in this landscape. That is, oxygen vacancy migration from {[]/O_{BZO}} \rightarrow {[]/O_{BZO}} and {O_{STO}/[]} \rightarrow {O_{STO}/[]} exhibit similar migration tendencies due to comparable nearest neighbor environment across the interface. The barrier height for a given vacancy to migrate in one direction and hop back to the same site (forward and backward jumps) is nearly equal except for the case where the vacancy is next to the dopants. Though the interface layers in the coherent terrace have somewhat more open space as compared to the grain interior, the migration barriers are comparable to those computed in the bulk.

Figure 3. Activation energy barriers for oxygen vacancy defect migration on the ZrO_2 side of the $SrO-ZrO_2$ interface. In (a), (b), and (c), two Gd^{3+} dopants are placed next to the oxygen vacancy in different locations. In (d), each Gd^{3+} dopant ion is isolated, but the total number of dopants and resultant oxygen vacancy concentration is consistent with previous configurations. Atomic color scheme is given below the figure panel and energy scale is given on the right for **Figures 3**, **4**, **5**, and **6**. The vacancy starting location is indicated with an open circle and misfit dislocations are indicated by dashed lines. View is normal to the interface, same as in **Figure 1**.

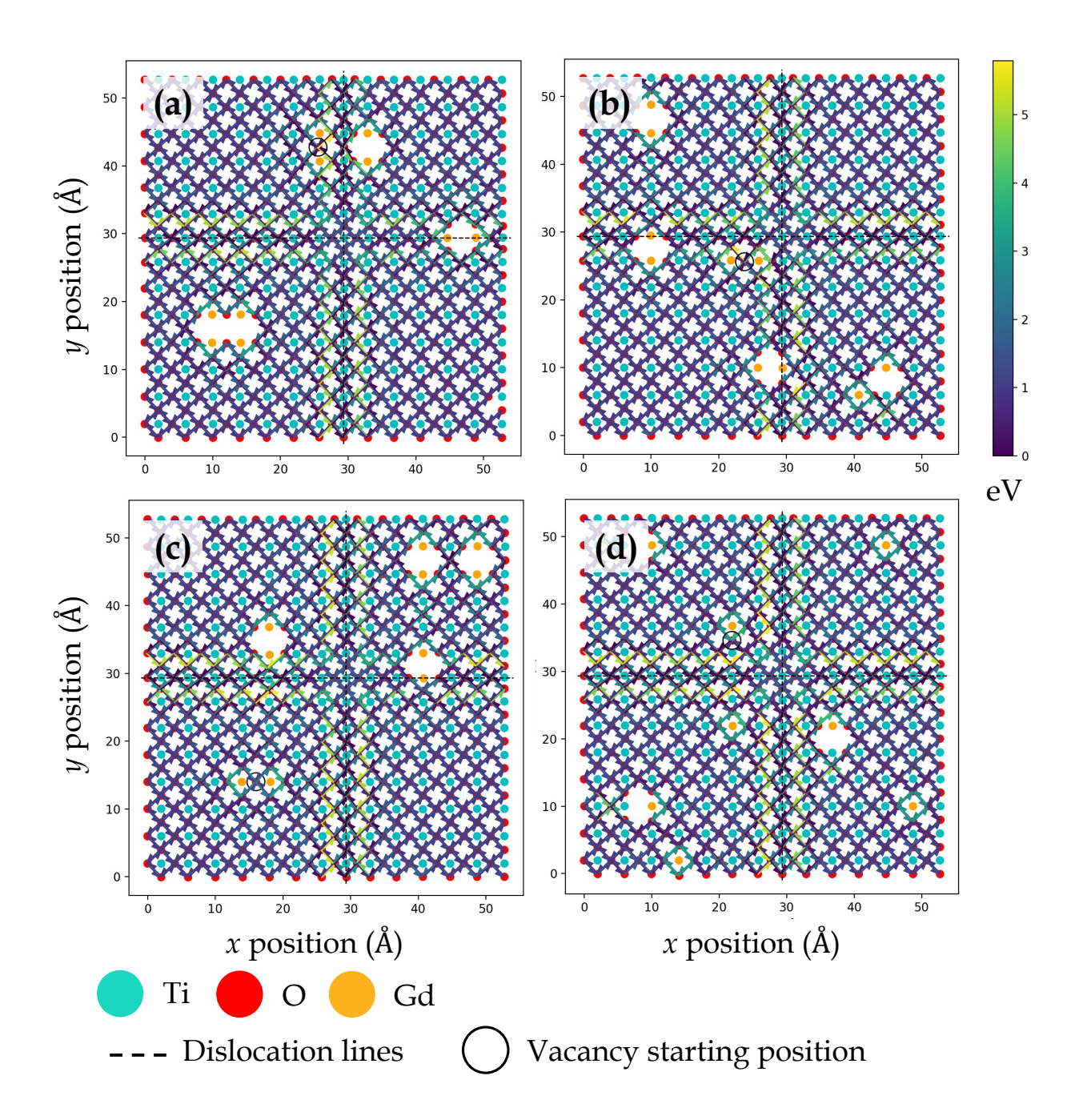


Near misfit dislocations in SrO–ZrO₂ and TiO₂–BaO interfaces, the migration tendencies of oxygen vacancies are different than those observed in the coherent regions. At SrO–ZrO₂ (**Figure 3**) and TiO₂–BaO (**Figure 4**) interfaces, oxygen vacancies exhibit lower activation energies migrating toward the misfit dislocations but higher energies migrating away from them. At the TiO₂–BaO interface, a characteristic difference emerges at the column of atoms next to misfit dislocations as oxygen vacancies reveal higher barriers migrating toward this column, but lower barriers migrating away from it, creating a distinct pattern in the spread of activation energies

near misfit dislocations. In general, this trend reveals that oxygen vacancies might get trapped since high thermal energy would be necessitated to overcome these barriers on either side of the column. The barriers for in-layer jumps across the misfit dislocations on the ZrO₂ side of SrO–ZrO₂ (**Figure 3**) interface were not computed because the jump distances involved are larger than next neighbor distances.

At TiO₂ and ZrO₂ side of the TiO₂–ZrO₂ interface, both layers across the interface have comparable chemical environments due to BO_2 – BO_2 interface chemistry. At ZrO₂ side (**Figure 5**) and TiO₂ side (Figure 6), oxygen vacancy migration in coherent terraces reveal a peculiar trait owing to oxygen ions having two types of nearest neighbor environment across the interface (Figure 1d). At the ZrO₂ side, the coherent terrace contains {Ti/O_{BZO}} and {[]/O_{BZO}} nearest neighbors, whereas at the TiO₂ side, it involves {O_{STO}/Zr} and {O_{STO}/[]}. At the ZrO₂ side, when oxygen vacancy migrates from neighborhood $\{Ti/O_{BZO}\} \rightarrow \{[]/O_{BZO}\},$ the migration barriers are low, but when it migrates from $\{[\]/O_{BZO}\} \rightarrow \{Ti/O_{BZO}\}$ or for the reverse jump, the migration barriers are high. An analogous trend is uncovered at the TiO₂ side, wherein the vacancy migration from neighborhood $\{O_{STO}/Zr\} \rightarrow \{O_{STO}/[\]\}$ involve low barriers, but the reverse jump or migration from $\{O_{STO}/[\]\} \rightarrow \{O_{STO}/Zr\}$ exhibit high barriers. Because one potential explanation for the observed trend can be offered on the basis of oxygen vacancy formation, we computed relative oxygen vacancy formation energies for a few cases at the interface layers in TiO₂–ZrO₂ interface. Oxygen vacancy formation was found to be significantly more favorable at neighborhoods $\{[]/O_{BZO}\}\$ and $\{O_{STO}/[]\}\$ as compared to $\{Ti/O_{BZO}\}\$ and $\{O_{STO}/Zr\}\$, respectively. Observed outcome is plausible since it is energetically favorable to remove an oxygen ion from a site where it has no nearest neighbor across the interface ({[]/O_{BZO}} or {O_{STO}/[]}) as compared to the location where it has a counterion ($\{Ti/O_{BZO}\}\)$ or $\{O_{STO}/Zr\}$) in an electrostatically favorable region. This result is in reasonable agreement with reported results for oxygen vacancy formation at oxide heterostructures. 54,55,56,68 The observed trend reveals a fundamental influence of interface layer chemistry on migration barriers since oxygen vacancies exhibit strong preference to migrate at sites that do not have nearest neighbor ions located across the interface.

Figure 4. Activation energy barriers for oxygen vacancy defect migration on the TiO_2 side of the $BaO-TiO_2$ interface. In (a), (b), and (c), two Gd^{3+} dopants are placed next to the oxygen vacancy in different locations. In (d), each Gd^{3+} dopant ion is placed isolated, but the total number of dopants and resultant oxygen vacancy concentration is consistent with previous configurations.



Oxygen vacancy migration trends in close proximity of misfit dislocations at both sides of the TiO₂–ZrO₂ interface are dissimilar than their respective coherent regions. At both ZrO₂ side (**Figure 5**) and TiO₂ side (**Figure 6**), lower activation energies are uncovered when oxygen vacancies hop toward the misfit dislocations, but higher activation energies are uncovered when they migrate away from them. For few oxygen ions bordering the misfit dislocations (hanging

oxygens in **Figure 5**) on the ZrO₂ side, a contrasting behavior is witnessed, wherein the activation energies are higher moving toward the misfit dislocations but lower moving away from them. However, once the vacancies move one jump distance from this location, they reach a site where all the barriers diffusing the vacancy away from it are noticeably higher. Essentially, the oxygen vacancies have a high likelihood of getting trapped at those sites. As stated earlier, the barriers for in-layer jumps across the misfit dislocations on the ZrO₂ side were not computed since these jump distances were larger than next nearest neighbor.

As compared to the coherent terraces, the discernable patterns in activation energy barriers emerging at misfit dislocations across the interfaces can be attributed to the atomic scale structure of misfit dislocations, which in turn depends on the interface layer chemistry as well as the concomitant strain at the interface. For instance, the respective interface layer arrangement of atoms in ZrO₂ (SI Figure S1b) and TiO₂ (SI Figure S1c) layers in SrO-ZrO₂ and TiO₂-BaO interfaces is noticeably different, which ultimately influence the pattern of activation energy barriers displayed in Figures 3 and 4. Since SrO-ZrO₂ and TiO₂-BaO interfaces exhibit misfit dislocations in the (100) crystal direction (Figure 1b and 1c), the variation in activation energies create a distinct pattern along the (100) direction. On the other hand, the respective interface layer arrangement of atoms in ZrO₂ (SI Figure S2d) and TiO₂ (SI Figure S2c) layers in TiO₂–ZrO₂ interface is dissimilar since the misfit dislocations are formed in the (110) direction (Figure 1d), which dictates the trend in activation energies depicted in Figures 5 and 6. The SrO-ZrO₂, TiO₂-BaO, and TiO₂–ZrO₂ interfaces exhibit a common behavior, wherein misfit dislocations push the interface layer atoms away from them, which creates somewhat larger space in their vicinity. This extra room makes it energetically favorable for larger oxygen ions to hop toward the misfit dislocations and less favorable to move away from them.

Figure 5. Activation energy barriers for oxygen vacancy defect migration on the ZrO_2 side of the TiO_2 – ZrO_2 interface. In (a), (b), and (c), two Gd^{3+} dopants are placed next to the oxygen vacancy in different locations. In (d), each Gd^{3+} dopant ion is placed isolated, but the total number of dopants and resultant oxygen vacancy concentration is consistent with previous configurations.

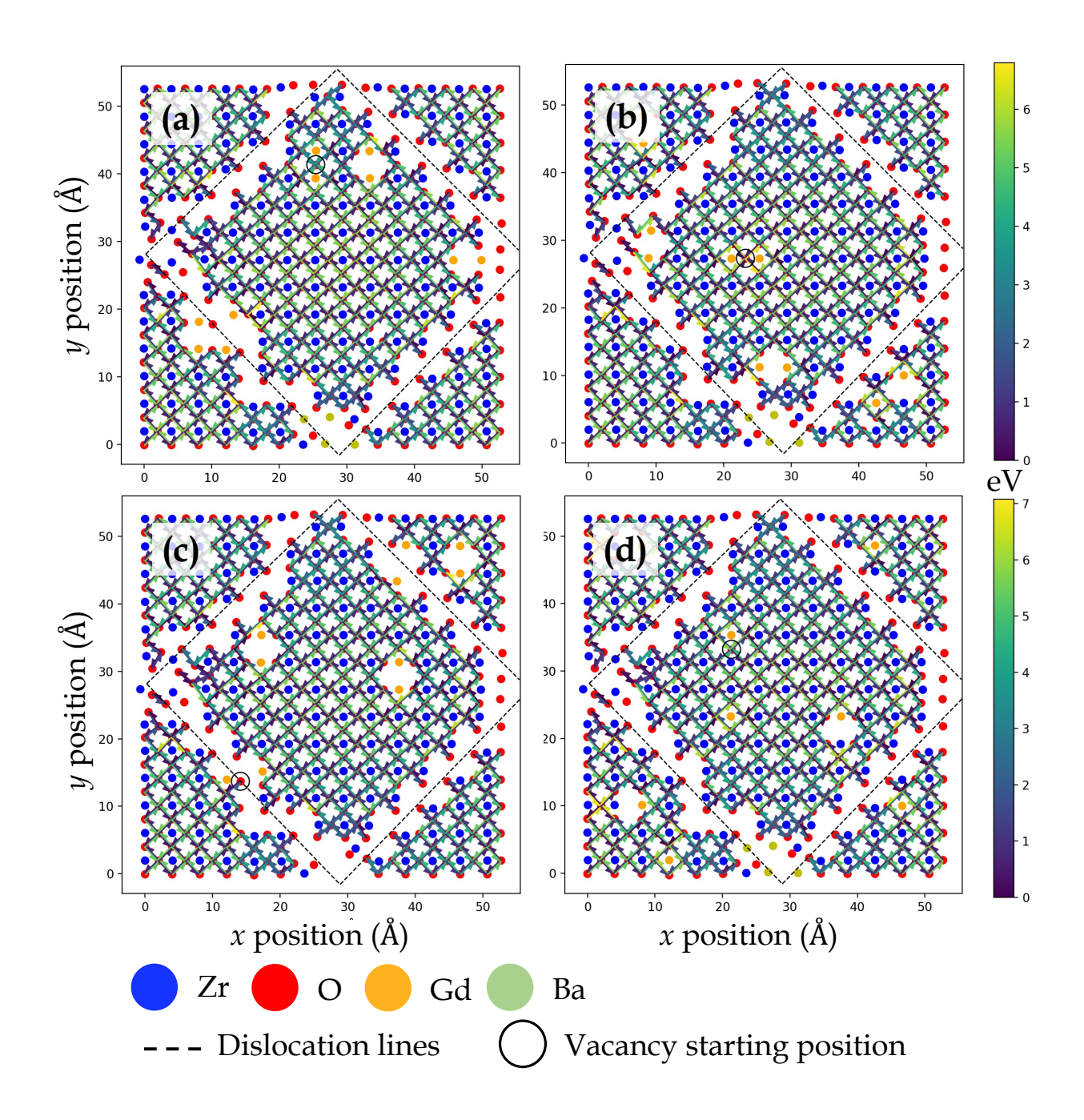
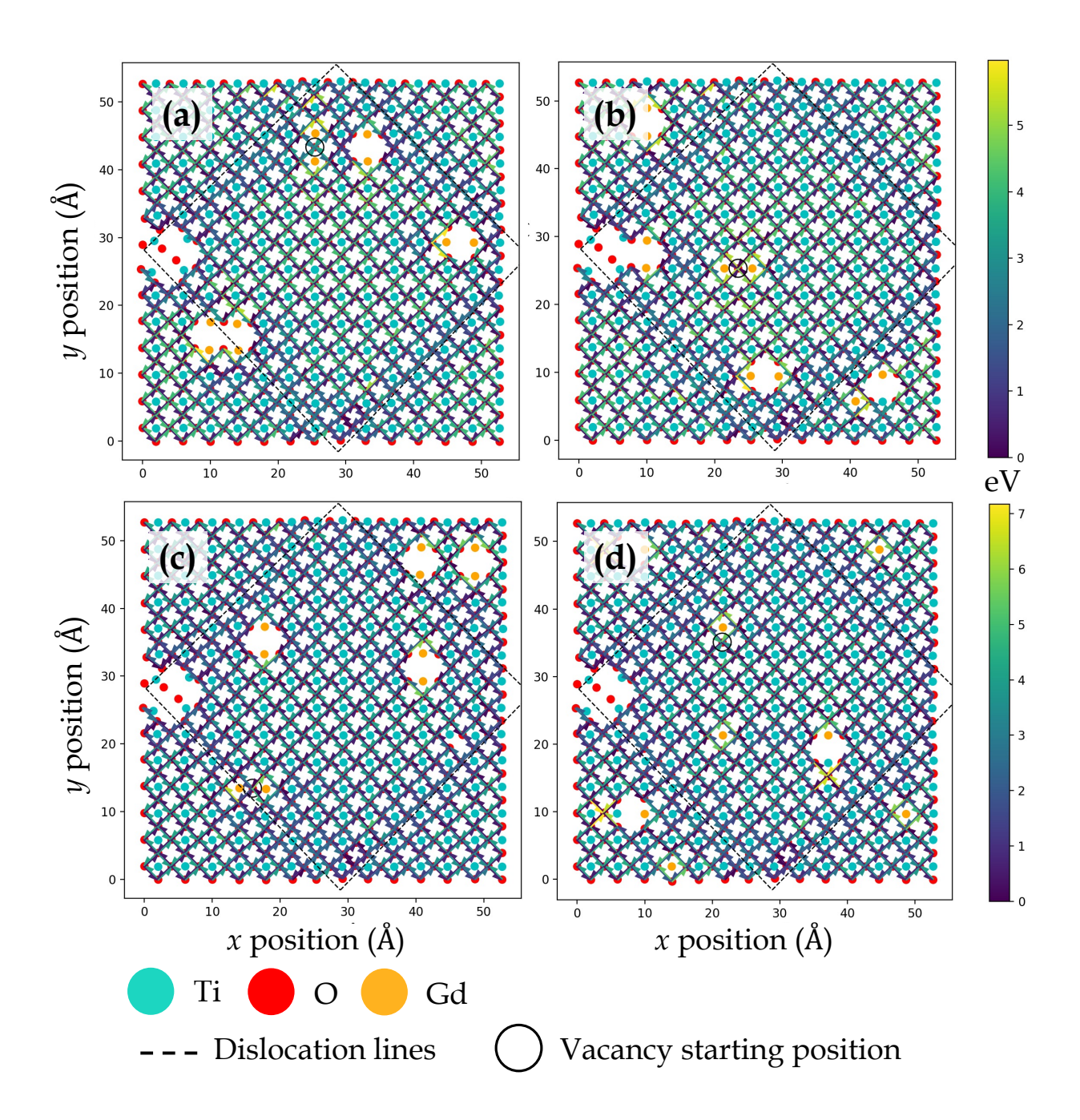


Figure 6. Activation energy barriers for oxygen vacancy defect migration on the TiO_2 side of the TiO_2 – ZrO_2 interface. In (a), (b), and (c), two Gd^{3+} dopants are placed next to the oxygen vacancy in different locations. In (d), each Gd^{3+} dopant ion is placed isolated, but the total number of dopants and resultant oxygen vacancy concentration is consistent with previous configurations.

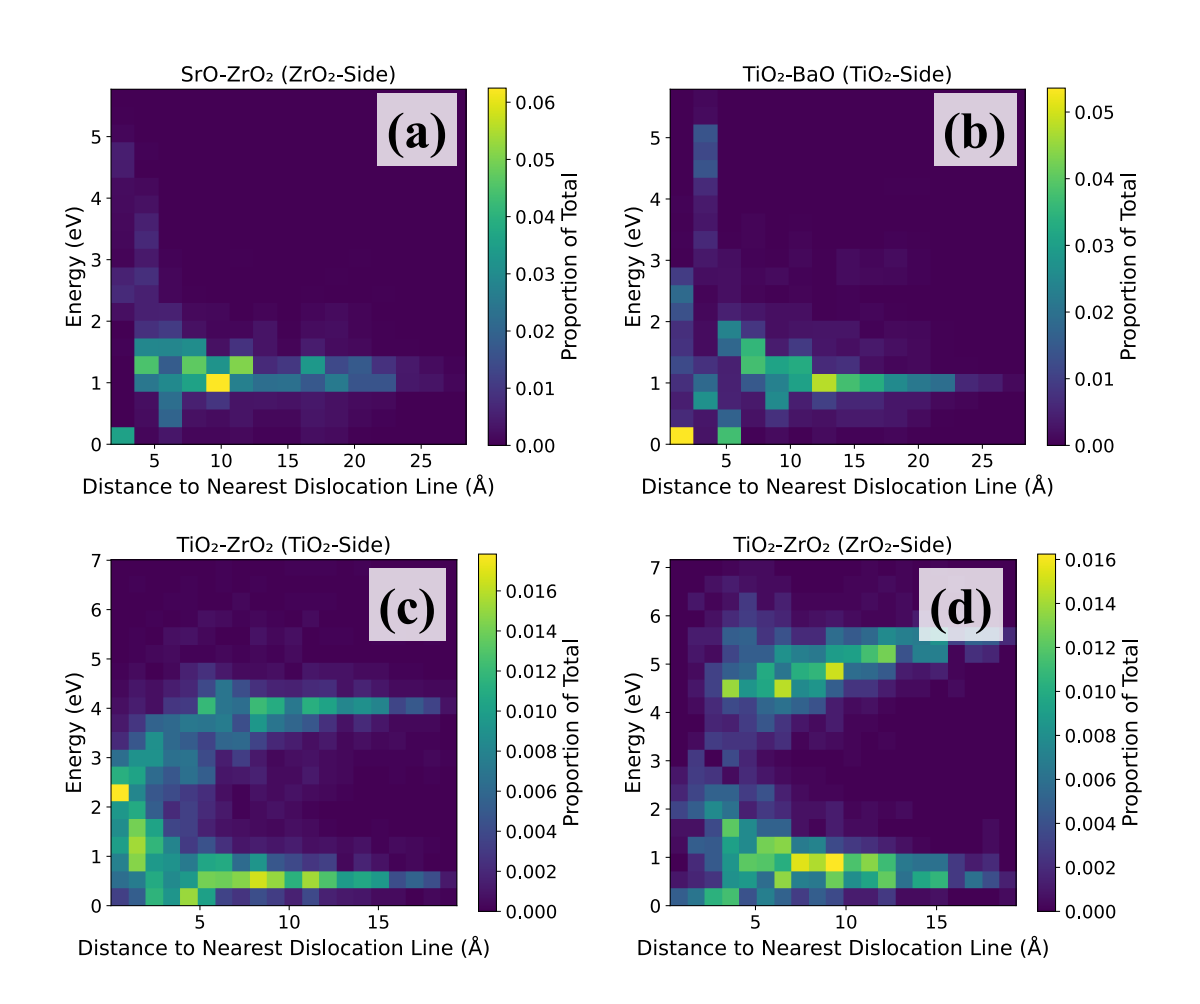


Since there are fewer atoms on the BZO side (13 unit cells) than the STO side (14 unit cells), there is a bit more room in the vicinity of misfit dislocations on the BZO side (**Figure S1** and **S2**), which further influences the observed trends. Select few calculations of relative oxygen vacancy formation at misfit dislocations reveal that they exhibit lower formation energies at misfit dislocations due to presence of chemically frustrated regions that are conducive to defect formation and availability of open space. Favorability of oxygen vacancy formation at misfit dislocations can also be inferred from activation energies for vacancy migration since these two quantities are

fundamentally correlated.⁸⁴ Because oxygen vacancy formation is energetically favorable at misfit dislocations in SrO–ZrO₂, TiO₂–BaO, and TiO₂–ZrO₂ interfaces, coupled with the effect that migration of these species toward misfit dislocations is favorable, a significant fraction of oxygen vacancies is expected in this locality. However, despite their higher concentration, these mobile species would have a lower probability of diffusing away from misfit dislocations owing to high activation barriers, which is likely to impact ionic transport in the vicinity of misfit dislocations.⁵⁵

Dopants display a noticeable influence on activation energies. Coherent regions in SrO-ZrO₂, TiO₂–BaO, and TiO₂–ZrO₂ interfaces that exhibit change in activation energies are primarily in the neighborhood of dopants, which in general lead to increase in activation energies. Placing the dopants in nearest neighbor pairs versus isolated do not have any significant impact on the migration behavior. Owing to electrostatic interactions and vacancy-dopant association, oxygen vacancies have low activation energy barriers to hop toward or between the two Gd3+ dopants in the coherent terrace (Figures 3c, 4c, 5b, and 6c) but would require higher thermal energy to move out of the vacancy-dopant complex. This behavior is uncovered at misfit dislocations as well, where the barriers to hop toward the two Gd³⁺ dopants are lower but hopping away are higher (Figures 3a, 3b, 4a, 4b, 5a, 5b, 6a, and 6c). To offer a glimpse of the distribution of energy barriers that exhibit highest, lowest, most accessible, and least accessible values at interface locations, 2D histograms for migration energy barriers at each of the four interfaces are given in Figure 7. Here, data is aggregated from all four scenarios performed for each particular interface layer and the distance is calculated using the migration pathway's closest point to the nearest dislocation line. Evidently, for the SrO-ZrO₂ and TiO₂-BaO interfaces, energy barriers remain fairly consistent (~1-1.5 eV), with some spread closer to the dislocation lines. For the TiO₂-ZrO₂ interface, an alternating pattern explained earlier is visible bit further from the dislocation lines, with the barrier value converging towards ~2-3 eV closer to misfit dislocations. In general, the SrO-ZrO2 and TiO2-BaO interfaces exhibit lower barriers. Largely, the influence of dopants in increasing the activation energies is more pronounced at misfit dislocations as compared to coherent terraces, a behavior in contrast with SOFC electrolytes, wherein trivalent dopants induce low energy pathways for vacancy migration in the grain interior of these materials. 85,86,87

Figure 7. 2D histograms for migration energy barriers at the four interfaces. Data is aggregated from all four scenarios performed for each particular interface layer. Distance is calculated using the migration pathway's closest point to the nearest dislocation line.



Literature work focused on examining the role of oxide interfaces for ionic conductivity applications have reported polarizing results. Several experiments have reported superionic conductivity in oxide heterostructures, 8,19,51,52,53,88,89 where misfit dislocations are hypothesized as potential pathways for fast ionic diffusion. On the contrary, few experiments have demonstrated that misfit dislocations slow down ionic transport in oxides. 90,91,92 Adding to the mystery are computational studies that report slower ionic diffusion at misfit dislocations 55 and dislocations lines in homophase oxides. 93,94 Nonetheless, the atomistic origin for this enhancement or impediment at misfit dislocations is not well understood. Fundamentally, analogous to the atomic arrangement uncovered in perovskite oxide heterostructures, mismatched oxide heterostructures

containing misfit dislocations at the interface are likely to have electrostatically balanced coherent terraces separated by misfit dislocations having chemically frustrated neighborhoods and complex atomic stacking. 54,57,60,68 As a result, atomic level insights offered herein for oxygen vacancy migration near misfit dislocations are germane to a broader class of mismatched oxide heterostructures. Dependence of activation energies on the atomic scale structure of misfit dislocations, especially as a function of interface layer chemistry, could be one of the fundamental factors responsible for reported inconsistences in ionic conductivity measurements. For instance, owing to the challenges involved in experimentally characterizing individual columns of misfit dislocations, it is likely that for the same thin film oxide heterostructure, 19,51,52,90,91,92 measurements performed for differing interface layer chemistry could yield varying ionic conductivity values since the dynamic behavior of oxygen vacancies would be altered as a function of atomic structure of misfit dislocations.

Present findings demonstrate a broad range of activation energies for oxygen vacancy defect migration at oxide interfaces that are contingent on the nearest neighbor environment and interface layer chemistry. This work sheds light on the intricacy associated with disentangling the fundamental aspects of oxide ion migration at mismatched oxide interfaces, which is noticeably different than that observed in the grain interior. Vitally, it suggests that to develop design principles for thin film oxide electrolytes with enhanced ionic conductivity, it is imperative to understand the atomic scale structure of extended defects at interfaces and study their influence on vacancy defect migration since basic understanding of bulk behavior is not sufficient. Lastly, it is essential to note that these results do not directly provide insights into diffusion kinetics. However, the rate of these events for nearest neighbor migration, that is the activation energies for oxygen vacancy migration at interfaces, can be incorporated in a KLMC model to study diffusion kinetics of oxygen vacancies as a function of temperature. To this end, a KLMC model is currently being developed in our group, which will utilize these input rates to simulate ionic conductivity at misfit dislocations in oxide heterostructures.

4. Conclusions

Formation and migration of oxygen vacancy defects at oxide interfaces is at the heart of the functioning of thin film oxide electrolytes. To this end, we have developed a high-throughput framework to predict the activation energy barriers for oxygen vacancy defect migration at misfit dislocations in perovskite oxide heterostructures. The present work offers a comprehensive account of activation energy barriers for diverse interface layer chemistries amid two lattice mismatched perovskite oxides. We have demonstrated the dependence of the migrating defect on nearest neighbor atomic environment across the oxide interface, which in turn is contingent on the atomic scale structure of misfit dislocations. Contrasting migration tendencies of oxygen vacancies were uncovered at coherent terraces as compared to misfit dislocations revealing the fundamental effect of extended defects on ionic transport. Activation energy barriers for vacancies hopping toward misfit dislocations exhibit lower magnitude, whereas moving away from them necessitates higher energy, indicating that oxygen vacancies would get trapped at misfit dislocations impacting ionic conductivity. Atomic scale insights offered herein pertaining to the energy landscape for oxygen vacancy migration at oxide interfaces will be instrumental in designing next-generation SOFC electrolytes, wherein the role of misfit dislocations at interfaces is central, but not well understood.

Conflicts of interest

There are no conflicts to declare.

Supporting Information: Interface atomic arrangements for STO and BZO layers in STO/BZO heterostructures for different interface chemistry.

Acknowledgements

This work is supported by the National Science Foundation (NSF) CAREER Award grant number 2042311 in the Division of Materials Research. The authors gratefully acknowledge resources from Research Computing at Rochester Institute of Technology. This work used Extreme Science and Engineering Discovery Environment (XSEDE), which is supported by NSF grant number ACI-1548562.

References

_

- ³ N. Pryds and V. Esposito. When Two Become One: An Insight into 2D Conductive Oxide Interfaces. *Journal of Electroceramics*, 2017, **38**, 1.
- ⁴ P. Yu, Y.-H. Chu, and R. Ramesh. Oxide Interfaces: Pathways to Novel Phenomena. *Materials Today*, 2012, **15**, 320.
- ⁵ Z. Huang, Ariando, X. R. Wang, A. Rusydi, J. Chen, H. Yang, and T. Venkatesan. Interface Engineering and Emergent Phenomena in Oxide Heterostructures. *Advanced Materials*, 2018, **30**, 1802439.
- ⁶ H. Y. Hwang, Y. Iwasa, M. Kawasaki, B. Keimer, N. Nagaosa, and Y. Tokura. Emergent Phenomena at Oxide Interfaces. *Nature Materials*, 2012, **11**, 103.
- ⁷ J. A. Kilner and M. Burriel. Materials for Intermediate-Temperature Solid-Oxide Fuel Cells. *Annu. Rev. Mater. Res.*, 2014, **44**, 365–393.
- ⁸ E. Fabbri, D. Pergolesi, and E. Traversa. Ionic Conductivity in Oxide Heterostructures: The Role of Interfaces. *Sci. Technol. Adv. Mater.*, 2010, **11**, 054503.
- ⁹ K. E. Sickafus, R. W. Grimes, J. A. Valdez, A. Cleave, M. Tang, M. Ishimaru, S. M. Corish, C. R. Stanek, and B. P. Uberuaga. Radiation-induced Amorphization Resistance and Radiation Tolerance in Structurally Related Oxides. *Nat. Mater.*, 2007, **6**, 217–223.
- ¹⁰ M. Salluzzo, S. Gariglio, D. Stornaiuolo, V. Sessi, S. Rusponi, C. Piamonteze, G. M. De Luca, M. Minola, D. Marré, A. Gadaleta, H. Brune, F. Nolting, N. B. Brookes, and G. Ghiringhelli. Origin of Interface Magnetism in BiMnO₃/SrTiO₃ and LaAlO₃/SrTiO₃ Heterostructures. *Phys. Rev. Lett.*, 2013, **111**, 087204.
- ¹¹ B. Zhu, L. Fan, and P. Lund. Breakthrough Fuel Cell Technology Using Ceria-based Multifunctional Nanocomposites. *Appl. Energy*, 2013, **106**, 163–175.
- ¹² J. Wang, G. Ji, Y. Liu, M. A. Gondal, and X. Chang. Cu₂O/TiO₂ Heterostructure Nanotube Arrays Prepared by an Electrodeposition Method Exhibiting Enhanced Photocatalytic Activity for CO₂ Reduction to Methanol. *Catal. Comm.*, 2014, **46**, 17–21.
- ¹³ B. C. H. Steele and A. Heinzel. Materials for Fuel-cell Technologies. *Nature*, 2001, **414**, 345.

¹ P. Zubko, S. Gariglio, M. Gabay, P. Ghosez, and J.-M. Triscone. Interface Physics in Complex Oxide Heterostructures. *Annual Reviews in Condensed Matter Physics*, 2011, **2**, 141.

² J. A. Sulpizio, S. Ilani, P. Irvin, and J. Levy. Nanoscale Phenomena in Oxide Heterostructures. *Annual Reviews in Materials Research*, 2014, **44**, 117.

¹⁴ A. Boudghene Stambouli and E. Traversa. Solid Oxide Fuel Cells (SOFCs): A Review of an Environmentally Clean and Efficient Source of Energy. *Renewable and Sustainable Energy Reviews*, 2002, **6**, 433.

- ¹⁵ S. C. Singhal and K. Kendall. *High-temperature Solid Oxide Fuel Cells: Fundamentals, Design and Applications*. Oxford: Elsevier, 2003.
- ¹⁶ E. D. Wachsman and K. T. Lee. Lowering the Temperature of Solid Oxide Fuel Cells. *Science*, 2011, **334**, 935.
- ¹⁷ A. Jaiswal, A. Pesaran, S. Omar, and E. D. Wachsman. Ceria/Bismuth Oxide Bilayer Electrolyte Based Low-Temperature SOFCs with Stable Electrochemical Performance. *ECS Transactions*, 2017, **78**, 361.
- ¹⁸ J. Santiso, J. Roqueta, N. Bagueś, C. Frontera, Z. Konstantinovic, Q. Lu, B. Yildiz, B. Martínez, A. Pomar, L. Balcells, and F. Sandiumenge. Self-Arranged Misfit Dislocation Network Formation upon Strain Release in La_{0.7}Sr_{0.3}MnO₃/LaAlO₃(100) Epitaxial Films under Compressive Strain. *ACS Appl. Mater. Interfaces* 2016, **8**, 16823–16832.
- ¹⁹ C. Korte, A. Peters, J. Janek, D. Hesse, and N. Zakharov. Ionic conductivity and activation energy for oxygen ion transport in superlattices—the semicoherent multilayer system YSZ-(ZrO₂ + 9.5 mol% Y₂O₃)/Y₂O₃. *Phys. Chem. Chem. Phys.*, 2008, **10**, 4623–4635.
- ²⁰ G. F. Harrington, A. Cavallaro, D. W. McComb, S. J. Skinner, and J. A. Kilner. The Effects of Lattice Strain, Dislocations, and Microstructure on the Transport Properties of YSZ Films. *Phys. Chem. Chem. Phys.*, 2017, **19**, 14319–14336.
- ²¹ D. Choudhury, B. Pal, A. Sharma, S. V. Bhat, and D. D. Sarma. Magnetization in Electronand Mn-doped SrTiO₃. *Sci. Rep.*, 2013, **3**, 1433.
- ²² R. A. Maier and C. A. Randall. Low-Temperature Ionic Conductivity of an Acceptor-Doped Perovskite: I. Impedance of Single-Crystal SrTiO₃. *J. Am. Ceram. Soc.*, 2016, **99** [10] 3350–3359.
- ²³ J. Cheng, Y. Wang, J. Luo, and K. Yang. δ-Doping Effects on Electronic and Energetic Properties of LaAlO₃/SrTiO₃ Heterostructure: First-Principles Analysis of 23 Transition-Metal Dopants. *Adv. Mater. Inter.*, 2017, **4**, 1700579.
- ²⁴ E. W. McFarland and H. Metiu. Catalysis by Doped Oxides. *Chem. Rev.*, 2013, **113**, 4391–4427.

²⁵ Y. Pai, A. Tylan-Tyler, P. Irvin, and J. Levy. Physics of SrTiO₃-based Heterostructures and Nanostructures: A Review. *Rep. Prog. Phys.*, 2018, **81**, 036503.

- ²⁶ W. Luo, W. Duan, S. G. Louie, and M. L. Cohen. Structural and Electronic Properties of *n*-doped and *p*-doped SrTiO₃. *Phys. Rev. B*, 2004, **70**, 214109.
- ²⁷ P. C. Bowes, J. N. Baker, and D. L. Irving. Survey of acceptor dopants in SrTiO₃: Factors limiting room temperature hole concentration. *J. American Ceram. Soc.*, 2020, **103**, 1156–11733.
- ²⁸ C. Y. R.Vera, H. Ding, D. Peterson, W. T. Gibbons, M. Zhou, and D. Ding. A mini-review on proton conduction of BaZrO₃-based perovskite electrolytes. *J. Phys. Energy*, 2021, **3**, 032019.
- ²⁹ P. P. Dholabhai, E. Martinez, and B. P. Uberuaga. Influence of Chemistry and Misfit Dislocation Structure on Dopant Segregation at Complex Oxide Heterointerfaces. *Adv. Theory Simul.* 2019, **2**, 1800095.
- ³⁰ S. Hui and A. Petric. Electrical Properties of Yttrium-Doped Strontium Titanate under Reducing Conditions. *J. Electro. Soc.*, 2002, **149**, J1–J10.
- ³¹ C. Ohly, S. Hoffmann-Eifert, K. Szot, and R. Waser. Electrical Conductivity and Segregation Effects of Doped SrTiO₃ Thin Films. *J. Eur. Ceram. Soc.*, 2001, **21**, 1673–1676.
- ³² D. V. Azamat, A. G. Badalyan, A. Dejneka, V. A. Trepakov, L. Jastrabik, and Z. Frait. High-frequency Electron Paramagnetic Resonance Investigation of Mn³⁺ Centers in SrTiO₃. *J. Phys. Chem. Solids* 2012, **73**, 822–826.
- H. Yang, H. S. Lee, P. G. Kotula, Y. Sato, Y. Ikuhara, and N. D. Browning. Amphoteric
 Doping of Praseodymium Pr³¹ in SrTiO₃ Grain Boundaries. *Appl. Phys. Lett.*, 2015, 106, 121904.
 L. Dai, L. Wu, H. Li, H. Hu, Y. Zhuang, and K. Liu. Evidence of the Pressure-induced
- ³⁵ R. Merkle and J. Maier. Defect Association in Acceptor-doped SrTiO3 : Case Study for Fe_{Ti}V_O and Mn_{Ti}V_O. *Phys. Chem. Chem. Phys.*, 2003, **5**, 2297–2303.

Conductivity Switching of Yttrium-doped SrTiO₃. J. Phys. Cond. Matt., 2016, 28, 475501.

- ³⁶ M. Longo, M. G. S. Costa, A. Z. Simoes, I. L. V.Rosa, C. O. P. Santos, J. Andres, E. Longo, and J. A. Varela. On the Photoluminescence Behavior of Samarium-doped Strontium Titanate Nanostructures Under UV Light. A Structural and Electronic Understanding. *Phys. Chem. Chem. Phys.*, 2010, **12**, 7566–7579.
- ³⁷ E. Gilardi, E. Fabbri, L. Bi, J. L. M. Rupp, T. Lippert, D. Pergolesi, and E. Traversa. Effect of Dopant–Host Ionic Radii Mismatch on Acceptor-Doped Barium Zirconate Microstructure and Proton Conductivity. *J. Phys. Chem. C*, 2017, **121**, 9739–9747.

³⁸ D. Han, K. Shinoda, S. Sato, M. Majimad, and T. Tetsuya Uda. Correlation between electroconductive and structural properties of proton conductive acceptor-doped barium zirconate. J. *Mater. Chem. A*, 2015, **3**, 1243.

- ³⁹ W. Lee, J. W. Han, Y. Chen, Z. Cai, and B. Yildiz. Cation Size Mismatch and Charge Interactions Drive Dopant Segregation at the Surfaces of Manganite Perovskites. *J. Am. Chem. Soc.*, 2013, **135**, 7909–7925.
- ⁴⁰ M. Shirpour, B. Rahmati, W. Sigle, P. A. van Aken, R. Merkle, and J. Maier. Dopant Segregation and Space Charge Effects in Proton-Conducting BaZrO₃ Perovskites. *J. Phys. Chem. C*, 2012, **116**, 2453–2461.
- ⁴¹ S. Chung, S. L. Kang, V. P. Dravid. Effect of Sintering Atmosphere on Grain Boundary Segregation and Grain Growth in Niobium-Doped SrTiO₃. *J. Am. Ceram. Soc.*, 2002, **85**, 2805–2810.
- ⁴² R. B. Wexler, G. S. Gautam, E. B. Stechel, and E. A. Carter. Factors Governing Oxygen Vacancy Formation in Oxide Perovskites. *J. Am. Chem. Soc.* 2021, **143**, 13212–13227.
- ⁴³ Q. Yang, J. X. Cao, Y. Ma, Y. C. Zhou, L. M. Jiang, and X. L. Zhong. Strain effects on formation and migration energies of oxygen vacancy in perovskite ferroelectrics: A first-principles study. *J. Appl. Phys.*, 2013, **113**, 184110.
- ⁴⁴ R. Merkle, Y. A. Mastrikov, E. A. Kotomin, M. M. Kuklja, and J. Maier. First Principles Calculations of Oxygen Vacancy Formation and Migration in Ba1–xSrxCo1–yFeyO3–δ Perovskites. *J. Electrochem. Soc.*, 2012, **159**, B219-B226.
- ⁴⁵ I. Kagomiya, K. Jimbo, K. Kakimoto, M. Nakayama, and Olivier Masson. Oxygen vacancy formation and the ion migration mechanism in layered perovskite (Sr,La)3Fe2O7. *Phys. Chem. Chem. Phys.*, 2014, **16**, 10875.
- ⁴⁶ J. M. Börgers and Roger A. De Souza. The surprisingly high activation barrier for oxygen-vacancy migration in oxygen-excess manganite perovskites. *Phys. Chem. Chem. Phys.* 2020, **22**, 14329.
- ⁴⁷ L. Zhang, B. Liu, H. Zhuang, P. R. C. Kent, V. R. Cooper, P. Ganesh, and H. Xu. Oxygen vacancy diffusion in bulk SrTiO3 from density functional theory calculations. *Comp. Mater. Sci.*, 2016, **118**, 309–315.
- ⁴⁸ J. J. Brown, Z. Ke, W. Geng, and A. J. Page. Oxygen Vacancy Defect Migration in Titanate Perovskite Surfaces: Effect of the A-Site Cations. *J. Phys. Chem.* C, 2018, **122**, 14590–14597.

⁴⁹ M. Cherry, M. S. Islam, and C. R. A. Catlow. Oxygen Ion Migration in Perovskite-Type Oxides. *J. Sol. State Chem.*, 1995, **118**, 125.

- ⁵⁰ Y. Pai, A. Tylan-Tyler, P. Irvin, and J. Levy. Physics of SrTiO₃-based Heterostructures and Nanostructures: A Review. *Rep. Prog. Phys.*, 2018, **81**, 036503.
- ⁵¹ M. Sillassen, P. Eklund, N. Pryds, E. Johnson, U. Helmersson, and J. Bøttiger. Low-temperature Superionic Conductivity in Strained Yttria-stabilized Zirconia. *Adv. Funct. Mater.*, 2010, **20**, 2071–2076.
- ⁵² J. Garcia-Barriocanal, A. Rivera-Calzada, M. Varela, Z. Sefrioui, E. Iborra, C. Leon, S. J. Pennycook, and J. Santamaria. Colossal Ionic Conductivity at Interfaces of Epitaxial ZrO₂:Y₂O₃/SrTiO₃ Heterostructures. *Science*, 2008, **321**, 676–680.
- ⁵³ S. M. Yang, S. Lee, J. Jian, W. Zhang, P. Lu, Q. Jia, H. Wang, T. W. Noh, S. V. Kalinin, and J. L. MacManus-Driscoll. Strongly Enhanced Oxygen Ion Transport Through Samarium-doped CeO₂ Nanopillars in Nanocomposite Films. *Nature Comm.* 2015, **6**, 8588.
- ⁵⁴ P. P. Dholabhai, G. Pilania, J. A. Aguiar, A. Misra, and B. P. Uberuaga. Termination Chemistry-driven Dislocation Structure at SrTiO₃/MgO Heterointerfaces. *Nature Comm.* 2014, **5**, 5043.
- ⁵⁵ P. P. Dholabhai, E. Martinez, N. T. Brown, and B. P. Uberuaga. On the Mobility of Carriers at Semi-coherent Oxide Heterointerfaces. *Phys. Chem. Chem. Phys.*, 2017, **19**, 23122.
- ⁵⁶ P. P. Dholabhai, J. A. Aguiar, A. Misra, and B. P. Uberuaga. Defect Interactions with Stepped CeO₂/SrTiO₃ Interfaces: Implications for Radiation Damage Evolution and Fast Ion Conduction. *J. Chem. Phys.*, 2014, **140**, 194701.
- ⁵⁷ P. P. Dholabhai, and B. P. Uberuaga. Beyond Coherent Oxide Heterostructures: Atomic-scale Structure of Misfit Dislocations. *Adv. Theory Simul.* 2019, **2**, 1900078.
- ⁵⁸ A. Lopez-Bezanilla, P. Ganesh, and P. B. Littlewood. Plentiful magnetic moments in oxygen deficient SrTiO3. *APL Mater.*, 2015, **3**, 100701.
- ⁵⁹ A. B. Muñoz-García, A. M. Ritzmann, M. Pavone, J. A. Keith, and E. A. Carter. Oxygen Transport in Perovskite-Type Solid Oxide Fuel Cell Materials: Insights from Quantum Mechanics. *Acc. Chem. Res.*, 2014, 47, 11, 3340.
- ⁶⁰ G. Pilania, P. P. Dholabhai, and B. P. Uberuaga. Role of Symmetry, Geometry, and Termination Chemistry on Misfit Dislocation Patterns at Semicoherent Heterointerfaces. *Matter*, 2020, **2**, 1324–1337.

⁶¹ S. Plimpton. Fast Parallel Algorithms for Short-range Molecular Dynamics. *J. Comput. Phys.*, 1995, **117**, 1–19.

- ⁶² R. A. Buckingham. The Classical Equation of State of Gaseous Helium, Neon and Argon. *Proc. R. Soc. London, Ser. A*, 1938, **168**, 264.
- ⁶³ P. P. Ewald. Evaluation of Optical and Electrostatic Lattice Potentials. *Ann. Phys.*, 1921, **64**, 253–287.
- ⁶⁴ G. Busker, A. Chroneos, R. W. Grimes, I. Chen. Solution Mechanisms for Dopant Oxides in Yttria. *J. Am. Ceram. Soc.*, 1999, **82**, 1553–1559.
- ⁶⁵ M. O. Zacate, L. Minervini, D. J. Bradfield, R. W. Grimes, K. E. Sickafus. Defect Cluster Formation in M₂O₃-doped Cubic ZrO₂. *Solid State Ionics*, 2000, **128**, 243–254.
- ⁶⁶ P. R. Choudhury and S. B. Krupanidhi. Dielectric response of BaZrO3/BaTiO3 and SrTiO3/BaZrO3 superlattices. J. Appl. Phys., 2008, **104**, 114105.
- ⁶⁷ N. A. Richter, S. Sicolo, S. V. Levchenko, J. Sauer, and M. Scheffler. Concentration of Vacancies at Metal-Oxide Surfaces: Case Study of MgO(100). *Phys. Rev. Lett.* 2013, **111**, 045502.
- ⁶⁸ P. P. Dholabhai. Oxygen Vacancy Formation and Interface Charge Transfer at Misfit Dislocations in Gd-Doped CeO₂/MgO Heterostructures. *J. Phys. Chem. C.*, 2022, **126**, 11735–11750.
- ⁶⁹ P. P. Dholabhai. Atomic-scale Structure of Misfit Dislocations in CeO₂/MgO Heterostructure and Thermodynamic Stability of Dopant-defect Complexes at the Heterointerface. *Phys. Chem. Chem. Phys.*, 2019, **21**, 20878.
- ⁷⁰ C. Marzano and P. P. Dholabhai, High-throughput prediction of thermodynamic stabilities of dopant-defect clusters at misfit dislocations in perovskite oxide heterostructures. *J. Phys. Chem. C*, **127**, 15988 (2023).
- ⁷¹ P. P. Dholabhai, R. Perriot, and B. P. Uberuaga. Atomic-Scale Structure and Stability of the Low-Index Surfaces of Pyrochlore Oxides. *J. Phys. Chem. C*, 2016, **120**, 10485.
- ⁷² Md. M. Hasan, P. P. Dholabhai, R. H.R. Castro, and B. P. Uberuaga. Stabilization of MgAl₂O₄ Spinel Surfaces Via Doping. *Surf. Sci.*, 2016, 649, 138–145.
- ⁷³ J. A. Aguiar, P. P. Dholabhai, Z. Bi, Q. Jia, E. G. Fu, Y. Q. Wang, T. Aoki, J. Zhu, A. Misra, and B.P. Uberuaga. Linking interfacial step structure and chemistry with locally enhanced

radiation- induced amorphization at oxide heterointerfaces. *Adv. Mater. Interfaces* 2014, **1(4)**, 1300142.

- ⁷⁴ P. P. Dholabhai, J. A. Aguiar, L. Wu, T. G. Holesinger, T. Aoki, R. H. R. Castro, and B. P. Uberuaga. Structure and Segregation of Dopant–defect Complexes at Grain Boundaries in Nanocrystalline Doped Ceria. *Phys. Chem. Chem. Phys.*, 2015, 17, 15375.
- ⁷⁵ R. Perriot, P. P. Dholabhai, and B. P. Uberuaga. Disorder-induced Transition from Grain Boundary to Bulk Dominated Ionic Diffusion in Pyrochlores. *Nanoscale*, 2017, **9**, 6826.
- ⁷⁶ M. M. Hasan, P. P. Dholabhai, S. Dey, B. P. Uberuaga, and R. H. R. Castro. Reduced Grain Boundary Energies in Rare-earth Doped MgAl2O4 Spinel and Consequent Grain Growth Inhibition. *J. Euro. Ceram. Soc.*, 2017, **37**, 40433.
- ⁷⁷ N. Kuwata, N. Sata, S. Saito, T. Tsurui, and H. Yugami. Structural and electrical properties of SrZr0.95Y0.05O3/SrTiO3 superlattices. Solid State Ionics, 2006, **177**, 2347–2351.
- ⁷⁸ P. P. Dholabhai, S. Anwar, J. B. Adams, P. Crozier, and R. Sharma. Kinetic lattice Monte Carlo model for oxygen vacancy diffusion in praseodymium doped ceria: Applications to materials design. *J. Sol. State Chem.*, 2011, **184**, 811–817.
- ⁷⁹ P. P. Dholabhai and J. B. Adams. A Blend of First-principles and Kinetic Lattice Monte Carlo Computation to Optimize Samarium-doped Ceria. *J. Mater. Sci.*, 2012, **47**, 7530.
- ⁸⁰ L. Zhang, B. Liu, H. Zhuang, P.R.C. Kent, V. R. Cooper, P. Ganesh, and H. Xu. Oxygen vacancy diffusion in bulk SrTiO3 from density functional theory calculations. *Comp. Mater. Sci.*, 2016, **118**, 309–315.
- ⁸¹ M. Schie, A. Marchewka, T. Müller, R. A. De Souza, and R. Waser. Molecular dynamics simulations of oxygen vacancy diffusion in SrTiO3. *J. Phys. Condens. Matter*, 2012, **24**, 485002.
- ⁸² J. Claus, M. Leonhardt, and J. Maier. Tracer diffusion and chemical diffusion of oxygen in acceptor doped SrTiO3. *J. Phys. Chem. Solids*, 2000, **61**, 1199–1207.
- ⁸³ B. P. Uberuaga and L. J. Vernon. Interstitial and vacancy mediated transport mechanisms in perovskites: A comparison of chemistry and potentials. *Solid State Ion.*, 2013, **253**, 18.
- ⁸⁴ S. L. Shang, B. C. Zhou, W. Y. Wang, A. J. Ross, X. L. Liu, Y. J. Hu, H. Z. Fang, Y. Wang, and Z. K. Liu A comprehensive first-principles study of pure elements: Vacancy formation and migration energies and self-diffusion coefficients. *Acta Mater.*, 2016, **109**, 128.
- ⁸⁵ D. A. Andersson, S. I. Simak, N. V. Skorodumova, I. A. Abrikosov, and B. Johansson. Optimization of Ionic Conductivity in Doped Ceria. *Proc. Natl. Acad. Sci.*, 2006, **103**, 3518.

⁸⁶ P. P. Dholabhai, J. B. Adams, P. Crozier, and R. Sharma. Oxygen Vacancy Migration in Ceria and Pr-doped Ceria: A DFT+*U* Study. *J. Chem. Phys.*, 2010, **132**, 094104.

- ⁸⁷ M. Nakayama and M. Martin. First-principles Study on Defect Chemistry and Migration of Oxide Ions in Ceria Doped with Rare-earth Cations, *Phys. Chem. Chem. Phys.*, 2009, **11**, 3241.
- ⁸⁸ Y. Saito, J. Cheng, K. Crabb, H. Huang, R. Pornprasertsuk, P. C. Su, and F. Prinz. Ion Conductivity Enhancement Effect by Introduction of Dislocations in Yttria-stabilized Zirconia. *ECS Transactions*, 2008, **11**, 3.
- ⁸⁹ S. Lee, W. Zhang, F. Khatkhatay, H. Wang, Q. Jia, and J. L. MacManus-Driscoll. Ionic Conductivity Increased by Two Orders of Magnitude in Micrometer-Thick Vertical Yttria-Stabilized ZrO₂ Nanocomposite Films. *Nano Letters*, 2015, **15**, 7362.
- ⁹⁰ X. Guo. Comment on Colossal Ionic Conductivity at Interfaces of Epitaxial ZrO₂:Y₂O₃/SrTiO₃ Heterostructures. *Science*, 2009, **324**, 465.
- ⁹¹ X. Guo, E. Vasco, S. Mi, K. Szot, E. Wachsman, and R. Waser. Ionic Conduction in Zirconia Films of Nanometer Thickness. *Acta Materialia*, 2005, **53**, 5161.
- ⁹² D. Pergolesi, E. Fabbri, S. N. Cook, V. Roddatis, E. Traversa, and J. A. Kilner. Tensile Lattice Distortion Does Not Affect Oxygen Transport in Yttria-Stabilized Zirconia CeO₂ Heterointerfaces. *ACS Nano*, 2012, 6, 10524.
- ⁹³ D. Marrocchelli, L. Sun, and B. Yildiz. Dislocations in SrTiO₃: Easy to Reduce but Not so Fast for Oxygen Transport. *J. Am. Chem. Soc.*, 2015, **137**, 4735.
- ⁹⁴ S. P. Waldow and R. A. De Souza. Computational Study of Oxygen Diffusion along a[100] Dislocations in the Perovskite Oxide SrTiO₃. *ACS Applied Materials and Interfaces*, 2016, **8**, 12246.